

# Black Phosphorus-Based Lithium-Ion Capacitor

Min Ju O,<sup>[a, b]</sup> Jun Hui Jeong,<sup>[a]</sup> Jong Hyeok Park,<sup>[b]</sup> Hyo-Jun Ahn,<sup>\*[c]</sup> and Kwang Chul Roh<sup>\*[a]</sup>

Black phosphorus (BP) with high theoretical capacity has received attention in lithium-ion capacitors (LICs). Nevertheless, it is difficult to introduce BP to LICs due to poor rate capability and cycling stability. In this study, we implement BP-based LIC by introducing BP/C composite with improved above mentioned problems. The composite exhibits capacities of 2156 and 1088 mAh g<sup>-1</sup> at 0.1 and 5.0 A g<sup>-1</sup>, respectively, and good cycling stability over 1000 cycles. It is the results of improved

electrical conductivity and mitigated volume expansion by embedded structure with BP in amorphous carbon and covalent bonding at interface. The LIC delivers maximum energy and power density of 178 Wh kg<sup>-1</sup> at 30 W kg<sup>-1</sup> and 3.0 kW kg<sup>-1</sup> at 65 Wh kg<sup>-1</sup>, respectively, and capacitance retention of 85% after 5000 cycles. The BP has been successfully introduced into LIC and has the ample potential for application in electric vehicles.

## Introduction

The rapid growth of the market for electric vehicles (EVs) has magnified the importance of energy storage devices with fast charging and cycling stability.<sup>[1,2]</sup> Supercapacitors (SCs), which deliver high power density and cycling stability, have received increasing attention in large energy storage devices.<sup>[3]</sup> Despite this interest, SCs suffer from the disadvantage of low specific energy due to the non-faradaic reactions at the surfaces of the electrodes. Recently, lithium-ion capacitors (LICs), in which the anodes are replaced with battery-type electrodes, have been intensively studied and developed.<sup>[4,5]</sup> The battery-type electrodes not only exhibit a higher capacity than supercapacitor-type electrode due to faradaic reactions at bulk region, but also has lower operating potential, which improves the capacity and working voltages of the LICs to implement high energy densities. LICs typically consist of carbonaceous materials (such as graphite, hard carbon, and soft carbon) which assist in rendering significantly higher energy densities than traditional SCs.<sup>[6–9,70]</sup> However, the energy densities of LICs are not sufficiently high for application in EVs owing to the limited specific capacity of carbonaceous materials

(<600 mAh g<sup>-1</sup>).<sup>[10,11]</sup> In addition, the faradaic reactions at the anode feature slower kinetics compared to the non-faradaic reactions at the cathode, resulting in a kinetic imbalance between the unsymmetrical electrodes, which negatively impacts the power density and cycling stability.<sup>[12–14]</sup> Therefore, LIC anode materials with considerably higher specific capacities than carbonaceous materials are necessary for achieving optimized rate capability and cycling stability.

Black phosphorus (BP) has recently received attention as an anode material principally because of its high theoretical capacity of 2596 mAh g<sup>-1</sup> ( $3\text{Li} + \text{P} \rightarrow \text{Li}_3\text{P}$ ) and appreciable electrical conductivity (~300 S m<sup>-1</sup>).<sup>[15–17]</sup> However, there are disadvantages that hinder the application of BP as an anode material in LICs. The Li<sub>3</sub>P alloy formed not only has poor electrical conductivity but also leads to the destruction of the crystal structure during delithiation.<sup>[18]</sup> In addition, Li<sub>3</sub>P is formed irreversibly and does not revert to BP.<sup>[19]</sup> This leads to a low initial coulombic efficiency (CE) and rate capability and decreased cycling stability. Moreover, the pulverization of particles due to the large volume change in phosphorus leads to the loss of electrical contact and continuously generates fresh surfaces during cycling, causing the decomposition of the electrolyte to form an unstable solid electrolyte interface (SEI) layer.<sup>[20,21]</sup> The resultant reduction in the availability of active sites for lithium-ion storage leads to the lowering of the specific capacity of the electrode material and the conductivity of the entire electrode through an increase in the contact resistance.<sup>[22,23]</sup> Mitigation of the aforementioned issues is crucial to enabling the application of BP as an anode material in LICs.

To address these issues, the development of nanocomposites with carbon materials, such as graphite, graphene, and carbon nanotubes (CNTs) has been reported.<sup>[24–27]</sup> These composites offer electrical conductivity and serve as buffer matrices which resist volume change, thus enhancing the rate capability and cycling stability. However, such approaches do not regard the problem of the reactivity of BP toward oxygen and moisture, which results in nano-sized BP with large surface area during electrode fabrication, leading to the loss of

[a] M. Ju O, Dr. J. Hui Jeong, Dr. K. Chul Roh  
Energy and Environment Division  
Korea Institute of Ceramic Engineering and Technology  
101 Soho-ro, 52851 Jinju-si, Gyeongsangnam-do, Republic of Korea  
E-mail: rk@kicet.re.kr

[b] M. Ju O, Prof. J. Hyeok Park  
Min Ju O, Jong Hyeok Park  
Department of Chemical and Biomolecular Engineering  
Yonsei University  
50 Yonsei-ro, Seodaemun-gu, 03722 Seoul, Republic of Korea

[c] Prof. H.-J. Ahn  
Hyo-Jun Ahn  
Department of Materials and Engineering  
Gyeongsang National University  
52828 Jinju-si, Gyeongsangnam-do, Republic of Korea  
E-mail: ahj@gnu.ac.kr

 Supporting information for this article is available on the WWW under  
<https://doi.org/10.1002/batt.202200031>

 An invited contribution to a Special Collection dedicated to Metal-Ion Hybrid Supercapacitors

electrochemically active sites. Therefore, BP nanocomposites incorporating carbon should be designed such that they not only offer a conductive matrix, but also provide protection to the BP surface against chemical degradation.<sup>[28–30]</sup> The incorporation of chemical bonds, such as P–C and P–O–C in the composites is considered a suitable strategy for surface passivation.<sup>[31–34]</sup> The presence of such bonds in the composite not only enhances its chemical stability, but also enables robust conductive contact, enhancing the interface stability of the composite. Moreover, it should be ensured that the composite structure securely encapsulates the increased surface area.<sup>[35–38]</sup> Thus, the design of BP composites as anode materials for LICs should include the aforementioned considerations.

As an anode material of LIC for high energy density, BP is required to improve rate capability and cycling stability. Herein, we implement a BP based LIC by synthesizing BP/C composite with the incorporation of chemical bonding in the embedded structure. The BP/C composite, which features BP nanoparticles embedded in a conductive amorphous carbon matrix, exhibits improved electrical conductivity, and prevents electrical disconnection through effective buffering. In addition, they exhibit high charge/discharge rates and repeatable reversible capacity. In particular, the presence of covalent bonding at the interface between BP and carbon ensures robust contact, thus offering mechanical stability during volume expansion, which supports long cycling stability. Moreover, the covalent bonding inhibits the chemical degradation of BP in the presence of moisture from the water-based binder used to support the severe volume change of the alloying materials during the electrode processes. Therefore, the BP/C composite, which delivers a combination of high capacity, optimized rate capability, and cycling stability with high initial CE could be introduced into

LICs to achieve LICs with high energy density that could potentially be used in EVs.

## Results and Discussion

The morphologies of the RP, BP, and BP/C composites were investigated using SEM. Irregular particle morphology was observed in RP with particle sizes of approximately 10–40 µm (Figure S1). After high energy milling, which is expected to cause the phase transformation of RP to BP, the particle size decreased to 100–300 nm (Figure 1a). In addition, the color of the powder changed from red to black (Figure S2), suggesting the phase transformation of RP to BP. The BP/C composite, obtained through additional high energy milling, exhibited agglomerated particles and a larger particle size than BP (Figure 1b and c). Impressively, the characteristic morphology of the one-dimensional (1D) structure of CNTs is not observed. The carbon present in the composite was observed via HAADF-EDS mapping (Figure S3). The EDS mapping images show uniform distribution of P and C elements in the composite, indicating the presence of both BP and CNTs. Moreover, the HAADF image exhibits a composite structure with BP embedded in the carbon. This suggests that the 1D structure of the CNTs was broken via high energy milling. To investigate in detail, the crystal lattice of the BP and CNTs, TEM was performed (Figure 1d). However, the crystal lattice of the BP and CNTs cannot be observed in the TEM image of the BP/C composite because the BP nanoparticles are surrounded by the fractured and amorphized CNTs. These results indicate that the secondary particles agglomerated with the nano-sized BP and

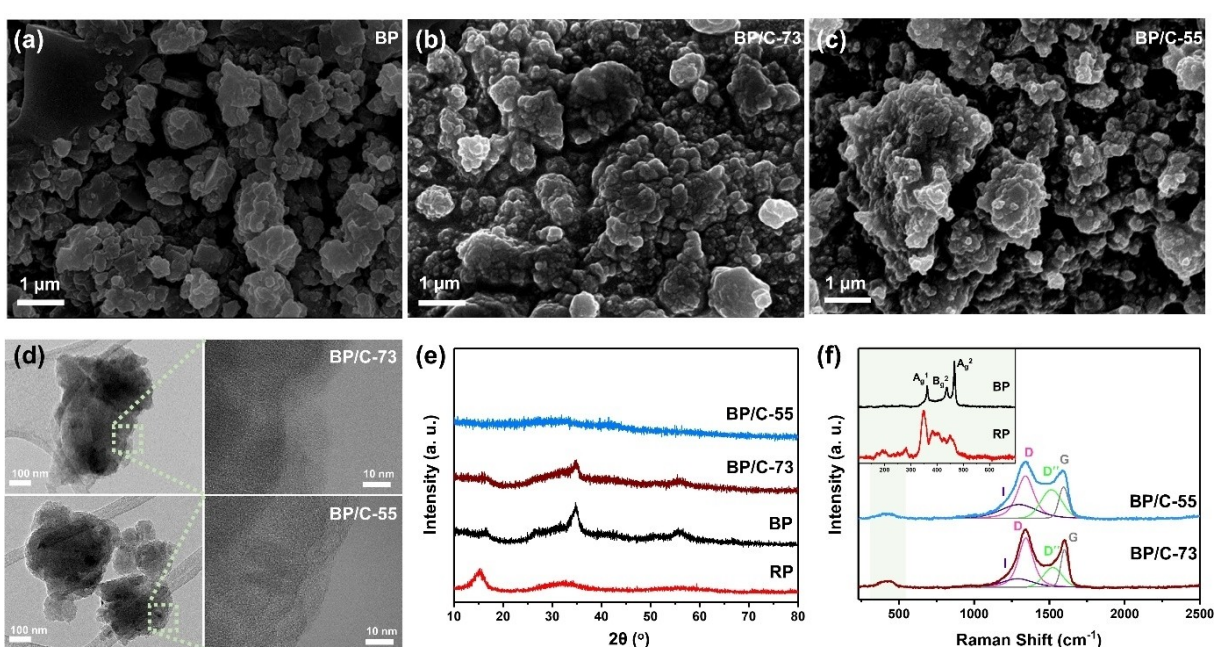


**Figure 1.** The structure and morphologies of BP/C composites prepared by high energy milling. SEM image of a) BP, b) BP/C-73, and c) BP/C-55. d) Low- and high-magnification TEM images of BP/C-73 and BP/C-55. e) XRD patterns and f) Raman spectra of RP, BP, BP/C-73, and BP/C-55.

amorphized CNTs have structures in which the BP is embedded in the amorphous carbon.

The changes in the crystal structures during high energy milling were investigated using XRD, and the results are shown in Figure 1(e). The XRD pattern of RP shows two characteristic peaks at 15° and 34°.<sup>[39]</sup> Following high energy milling, the two peaks corresponding to RP disappeared and the three peaks at 26°, 35°, and 55° appeared, which correspond to the orthorhombic phase of BP (standard diffraction file JCPDS #00-009-0020). Both the BP/C composites prepared using different CNT contents show broadened peaks compared to those of BP. The BP contents in the composites were measured to be 71% and 48% for BP/C-73 and BP/C-55, respectively, using TGA (Figure S4). With increasing carbon contents, a reduction in the intensity of the peaks corresponding to BP was observed, suggesting that the BP nanoparticles are shielded by the amorphous carbon. As predicted from the SEM and TEM images, the characteristic peaks of CNTs at 26° and 43° (Figure S5a) are not detected because the CNTs are fractured and amorphized by high energy milling.<sup>[40,41]</sup> The phase transformation of RP to BP is attributed to the high energy milling, which is responsible for the reduction in the particle size. The embedded structure in the amorphous carbon provides a 3D conductive path matrix and effective buffering that accommodates volume expansion.

Raman spectroscopy was used to characterize the structure of the BP and CNT in the composite, as shown in Figure 1(f). The Raman spectrum of BP shows three peaks corresponding to the  $A_g^1$ ,  $B_g^2$ , and  $A_g^2$  vibration modes at 363, 440, and  $467\text{ cm}^{-1}$ , respectively.<sup>[42,43]</sup> These modes represent the vibrations of the P–P bond in three directions. The CNTs exhibited Raman bands centered at 1340 and  $1599\text{ cm}^{-1}$  designated as the D and G bands, respectively (Figure S5b).<sup>[44]</sup> The D band represented defects in the graphitic structure, whereas the G band indicated the degree of graphitization.<sup>[45]</sup> The BP/C composites showed characteristic peaks of BP and carbon. As the proportion of CNT in the composite increased, the intensity of the peak corresponding to BP decreased and that of the peak at  $\sim 1500\text{ cm}^{-1}$  increased. The decreased intensity of the peaks corresponding to BP indicated that the P–P bonding is broken due to the reduction in particle size and formation of new functionalities on the BP surface during high energy milling. The range of  $750\text{--}2050\text{ cm}^{-1}$  is deconvoluted four peak including D and G peak at 1340 and  $1599\text{ cm}^{-1}$  to confirm detail characterization of carbon. I band at  $1295\text{ cm}^{-1}$  is normally attributed to the  $\text{sp}^2\text{--}\text{sp}^3$  bonds, disorder in the graphitic lattice and the D'' band at  $1525\text{ cm}^{-1}$  is related to the presence of amorphous carbon.<sup>[46]</sup> The intensity of the peak at  $1525\text{ cm}^{-1}$  is stronger in BP/C-55, which has a relatively high carbon content, that means have a large amount of amorphous carbon. The intensity ratios of the D bands to those of the G bands ( $I_D/I_G$ , an indicator of the degree of conjugation disruption) for the BP/C-73 and BP/C-55 composites equaled 1.31 and 1.48, respectively. The  $I_D/I_G$  values for the BP/C composites were higher than that of pristine CNTs (1.07), indicating that the CNTs in the composites had disordered structures and high defect densities.<sup>[47]</sup> These results confirmed

the introduction of defects in the CNTs in the composite by the high energy milling process. Increasing the CNT content in the composite corresponds to larger proportions of amorphous carbon. The particle size of BP was reduced, and the CNT was transformed to amorphous carbon by high energy milling, leading to a lowering of the chemical energy barrier. These results suggest that new chemical interactions were facilitated on the BP surface.

Chemical interaction is important to improve the chemical and mechanical stability of BP. The covalent bonds between phosphorus and the carbon interface were identified using XPS. The presence of phosphorus and carbon were confirmed from the XPS survey spectra of the BP/C composites (Figure S6). The peaks associated with C 1s and P 2p at their corresponding binding energies of 283–290 and 130–137 eV, respectively, are demonstrated. The presence of chemical bonds between phosphorus and carbon is also evidenced in the C 1s spectra shown in Figure 2(a–c). The CNTs (Figure 2a) showed peaks at 283.6, 284.8, and 285.5–290.5 eV corresponding to  $\text{sp}^2\text{C}$ ,  $\text{sp}^3\text{C}$ , and multiple groups, such as carboxyl, hydroxyl, and carbonyl, respectively.<sup>[48]</sup> The presence of  $\text{sp}^2\text{C}$  denotes the C=C bond, indicating graphitic carbon, and  $\text{sp}^3\text{C}$  corresponds to the C–C bond, indicating disordered carbon.<sup>[49]</sup> The CNTs in the composite showed a decrease in the proportion of  $\text{sp}^2\text{C}$  and an increase in that of  $\text{sp}^3\text{C}$  compared to the pristine CNT, which showed a dominant  $\text{sp}^2\text{C}$  peak. Notably, an additional peak at 282.8 eV appeared corresponding to the P–C bond.

The XPS P 2p spectra of BP and the composites are shown in Figure 2(d–f). The P 2p spectrum of the as-prepared BP shows peaks at 130.4 and 130.8 eV corresponding to  $\text{P}2\text{p}_{3/2}$  and  $\text{P}2\text{p}_{1/2}$ , respectively, due to P–P bonding, which indicates the presence of unreacted BP ( $\text{P}^0$ ).<sup>[50]</sup> A tiny peak at 133.7 eV characteristic of P=O and P–O bonds was detected, indicating the formation of a thin oxide layer on the surface of the as-prepared BP during high energy milling.<sup>[51]</sup> After high energy milling, the BP/C composites showed a significant reduction in the intensity of the peak representing the P–P bond. However, two additional peaks emerged at 129.4 and 131.2 eV, corresponding to  $\text{P}2\text{p}_{3/2}$  and  $\text{P}2\text{p}_{1/2}$ , respectively, due to P–C bonding, indicating the formation of P–C bonds through connection between the BP and amorphous carbon.<sup>[52,53]</sup> A decrease in P–P bonding is observed with decreasing the CNT content, whereas P–C bonding is increased. Because new interaction can be more readily formed between damaged carbon and BP. Covalent bonding like P–C bonding is strong interaction, leads to maintain electrical contact between phosphorus and carbon in large volume expansion. Moreover, increasing the CNT content in BP/C composites shifted the peak to a lower binding energy of approximately 133.7 eV with increasing intensity. These results did not suggest the formation of continuous oxidation passivation but the formation of P–O–C bonds, which provide chemical stability to BP.<sup>[54,55]</sup> TGA was performed to investigate the chemical stability of the P–C and P–O–C bonding (Figure S4). The TGA curves of the BP/C composites display a weight loss step at  $\sim 450^\circ\text{C}$  due to the thermal decomposition of the physically adsorbed BP.<sup>[56]</sup> The sublimation temperature of the BP/C composites increased

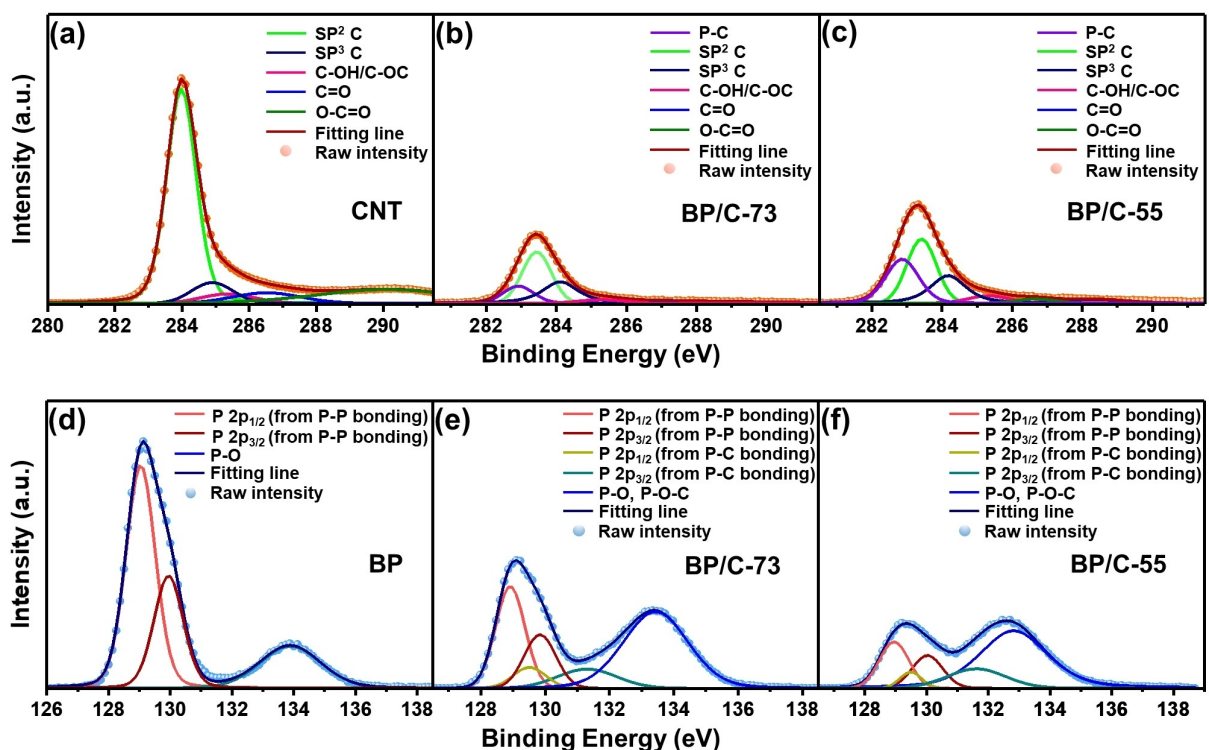


**Figure 2.** The existence of P–C and P–O–C bonding in BP/C composites. High-resolution C 1s XPS spectra of a) CNT, b) BP/C-73, and c) BP/C-55. High-resolution P 2p XPS spectra of d) BP, e) BP/C-73, and f) BP/C-55.

gradually with increasing CNT content, indicating enhanced structural and thermal stability due to P–C and P–O–C bonding. These results for the BP/C composites indicate an increase in the structural disorder and a reduction in the energy barrier to chemical reactions, which contributed to the formation of P–C and P–O–C bonds. The occurrence of these bonds was confirmed in both the composites, and high CNT contents led to enhanced chemical bonding. According to these results, the enhanced chemical and mechanical stability of BP in the composite leads to robust contact with the buffer matrix, enabling continuous charge/discharge.

The rationally designed BP/C composite is expected to impart electrical conductivity and prevent electrical disconnection by virtue of an effective buffer matrix structure. In addition, it must exhibit a high rate of charge/discharge and repeatable reversible capacity. The electrochemical performance of the BP/C composites was evaluated using a lithium metal half-cell under the following conditions: 1 M LiPF<sub>6</sub> electrolyte solution in 1:1 EC/DMC with FEC as the additive in the potential window of 0.01–2.0 V (vs. Li/Li<sup>+</sup>). The specific capacities of the composites were calculated based on the weights of BP in the composites because the capacity of CNTs is negligible in the potential window investigated in this study.

The first GCD profiles of BP, BP/C-73, and BP/C-55 are shown in Figure 3(a). Under lithiation, all the samples exhibited a broad shoulder at approximately 1.30–0.95 V (vs. Li/Li<sup>+</sup>), which was primarily due to the irreversible reaction forming the SEI layer.<sup>[57,58]</sup> BP exhibited a wide plateau region at 0.75 V while the BP/C composites showed a slightly sloping plateau

region (0.75–0.60 V), which resulted from the decreased particle size of BP caused by high energy ball milling. BP/C-73 and BP/C-55 delivered first discharge capacities of 3031 and 2507 mAh g<sup>-1</sup>, respectively, and their initial CEs were calculated to be 85% and 86%, respectively. The initial CE of BP (8%) is much lower than those of the BP/C composites, which is attributed to the loss of electrical contact after cracking, as well as the poor electronic conductivity of Li<sub>3</sub>P. Thus, BP/C-73 and BP/C-55 delivered second discharge capacities of 2294 and 2035 mAh g<sup>-1</sup>, respectively, while BP delivered a very low reversible capacity of 207 mAh g<sup>-1</sup> (Figure 3b). Moreover, the BP/C composites in the second cycle under lithiation did not show a plateau region at 1.30–0.95 V owing to the formation of the SEI layer, resulting in improved CEs of 96% and 95% for BP/C-73 and BP/C-55, respectively. BP/C-55 had a more pronounced sloping plateau region (0.75–0.60 V) than BP/C-73, as suggested by the combined sloping characterization of the GCD profiles of the CNTs (Figure S7) in the composites. These results indicate that the embedded structure of the nano-sized BP in the carbon matrices imparted interface stability to the BP via formation of a uniform SEI layer in the first cycle.

The rate capabilities of BP/C-73 and BP/C-55 are shown in Figure 3(c). BP/C-73 exhibited discharge capacities of 2205, 2050, 1903, and 1745 mAh g<sup>-1</sup> at 0.1, 0.2, 0.5, and 1.0 Ag<sup>-1</sup>, respectively. BP/C-55 achieved discharge capacities of 1810, 1703, 1475, and 1296 mAh g<sup>-1</sup> at current densities of 0.1, 0.2, 0.5, and 1.0 Ag<sup>-1</sup>, respectively. At a high current density of 5.0 Ag<sup>-1</sup>, BP/C-73 and BP/C-55 exhibited 58.9% and 60.1% retention of their initial discharge capacities at 0.1 Ag<sup>-1</sup>,

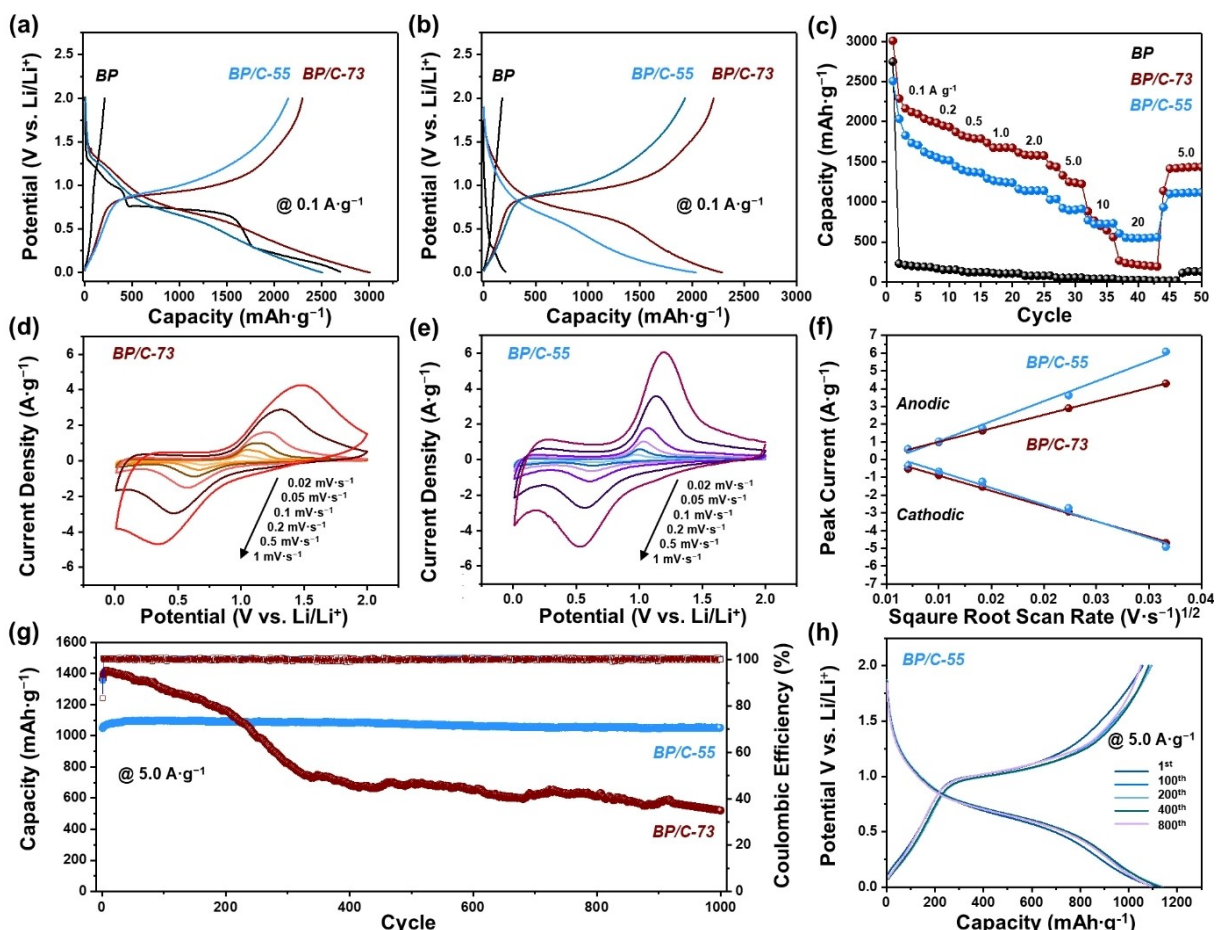


**Figure 3.** Electrochemical performance of BP and BP/C composites using a lithium-metal half-cell. a) The first and b) second GCD profiles of BP, BP/C-73, and BP/C-55 at  $0.1 \text{ A g}^{-1}$ . c) Rate capability of BP, BP/C-73, and BP/C-55 at various current densities (increased from  $0.1$  to  $20 \text{ A g}^{-1}$ ). CV at various scan rates (increased from  $0.02$  to  $1 \text{ mV s}^{-1}$ ) of d) BP/C-73 and e) BP/C-55. f) Linear relationship between the peak current and square root of the scan rate fitted to the Randles-Sevcik equation for BP/C-73 and BP/C-55. g) Cycling stability of BP/C-73 and BP/C-55 at a current density of  $5.0 \text{ A g}^{-1}$  and h) the corresponding GCD profiles for 1, 100, 200, 400, and 800 cycles at  $5.0 \text{ A g}^{-1}$  of BP/C-55.

respectively. The carbon present in the composites acts as a buffer matrix and is responsible for their electrical conductivity, thus enhancing the rate capability. Interestingly, at a high current density of  $20 \text{ A g}^{-1}$ , BP/C-55 retained 30.1% of its initial discharge capacity at  $0.1 \text{ A g}^{-1}$ , while BP/C-73 retained 10.4%. In particular as the current density was increased from  $0.1 \text{ A g}^{-1}$  to  $20 \text{ A g}^{-1}$ , the discharge capacities of BP/C-55 and BP/C-73 diminished progressively from  $1810$  to  $544 \text{ mAh g}^{-1}$  and from  $2205$  to  $230 \text{ mAh g}^{-1}$ , respectively. BP/C-55 exhibited higher rate capability at high current densities because its high carbon content led to enhanced formation of stable covalent bonds, enabling strong adhesion to the conductive buffer matrix while maintaining sufficient electrical contact. CV tests were performed at different scan rates to better understand the enhanced rate capability. The reduction peaks observed at  $0.68$  and  $0.01 \text{ V}$  on the cathodic scan correspond to the formation of  $\text{Li}_x\text{P}$  ( $x=1-3$ ).<sup>[59]</sup> On the anodic scan, the oxidation peaks at  $0.12$  and  $0.98 \text{ V}$  occur due to the delithiation process.<sup>[60]</sup> The potential at which the redox peaks appeared in the CV profiles corresponded to the plateau region in the GCD profiles. The CV curves of BP/C-55 show similar peaks during the cathodic and

anodic processes at an increased scan rate. Upon increasing the scan rate, the BP/C-55 composite exhibits a minor peak shift compared to BP/C-73, indicating relatively lower polarization.

Moreover, the improved rate capabilities of the BP/C composites were closely related to their  $\text{Li}^+$  transport abilities, which were estimated using the CV curves (Figure 3d and e) according to the Randles-Sevcik equation. Figure 3(f) shows the plots for  $I_p$  and  $(V \text{ s}^{-1})^{1/2}$  ( $I_p$  is the peak current, and  $V \text{ s}^{-1}$  is the scan rate), which show a linear relationship. The slope of the curves suggests fast  $\text{Li}^+$  transport abilities.<sup>[61]</sup> Both the BP/C composites have similar slopes for the lithiation process, while the slope of BP/C-55 is steeper than that of BP/C-73 for the delithiation process. Particularly, the  $\text{Li}_3\text{P}$  alloy is formed during delithiation, which has poor electrical conductivity and leads to the destruction of the crystal structure. These results show that electrically conductive paths were maintained, and pulverization was mitigated during delithiation due to sufficient electrical contact and strong chemical bonding at the interface between phosphorus and carbon, which were induced by the higher CNT contents.

The cycling stability of BP/C-73 and BP/C-55 was studied at  $5.0 \text{ A g}^{-1}$  (Figure 3g). BP/C-55 presented superior cycling stability up to 1000 cycles with a capacity of  $1088 \text{ mAh g}^{-1}$  and an initial capacity retention of 98%, while BP/C-73 delivered a capacity of  $520 \text{ mAh g}^{-1}$  and an initial capacity retention of 43%. Notably, BP/C-73 exhibits capacity fading from 1180 to  $740 \text{ mAh g}^{-1}$  near the 400<sup>th</sup> cycle. To elucidate the cycling stability of BP/C-55, the GCD profiles for the cycles were studied (Figure 3h). A comparison between the GCD profiles for the 200<sup>th</sup> and 400<sup>th</sup> cycles of BP/C-73 show a markedly increased overpotential and truncated plateau region (Figure S8). Meanwhile, the GCD profiles of BP/C-55 were found to be stable not only at the 400<sup>th</sup> cycle but also at the 800<sup>th</sup> cycle with a slight increase in the overpotential. These results suggest that high carbon contents lead to increased P–C and P–O–C bonding, enhancing the mechanical stability of BP as well as the stability of the composite structure due to strong interaction between the interface of BP and the buffer matrix. In addition, the CE of BP/C-73 and BP/C-55 was maintained at ~100% for up to 1000 cycles.

It was reported that the capacity of an LIC improves until the anode capacity reaches  $1200 \text{ mAh g}^{-1}$ , beyond which it becomes negligible because of the low specific capacity of the AC cathode.<sup>[62]</sup> Therefore, for anode materials with a high specific capacity of  $1200 \text{ mAh g}^{-1}$  or above, their rate capability and cycling stability should be considered before their application in high performance LICs. Because these results demonstrate the noticeably enhanced cycling stability and rate capability of the BP/C-55 compared to BP/C-73, the former was chosen for use as an LIC anode material.

LIC full cell, which is asymmetric cell with different charge storage mechanism each negative and positive electrode requires capacity balancing both electrodes to optimize high energy and power density. The capacity balancing of LIC is affected by the specific capacity of each electrode, the active mass of the electrode material, and the working potential window. The points to special considered is finding the optimal capacity balancing at various current density, due to kinetic mismatch between faradaic lithiation/delithiation in negative electrode and non-faradaic adsorption/desorption in positive electrode. To set the negative electrode to positive electrode mass ratio for the LIC, the half-cell composed of AC and lithium metal as the counter electrode was fabricated and the specific capacity of BP/C-55 was measured at various current densities (increased from 0.1 to  $5.0 \text{ mA cm}^{-2}$ ), as shown in Figure S9. The working potential windows are set of negative electrode 0.05–2.0 V and positive electrode 2.5–4.3 V. Thus, three LIC cells were assembled using electrodes of the investigated mass ratios 1:14, 1:17, and 1:20 (being  $m_{\text{NE}}:m_{\text{PO}}$ ) at various current densities. The electrochemical performance of the BP/C-55//AC 1:14, 1:17, and 1:20 was evaluated using a full-cell under the following conditions: 1 M LiPF<sub>6</sub> electrolyte solution in 1:1 EC/DMC with FEC as the additive in the voltage range of 0.5–4.3 V. The result of mass ratio that can maximize energy and power density is BP/C-55//AC 1:17, as shown Figure S10.

Figure 4 shows the electrochemical performance of BP/C-55//AC set to the optimal mass ratio. The specific capacitances

of the BP-based LIC were calculated based on the total masses of the anodic and cathodic active materials. The GCD profiles of BP/C-55//AC show under different current densities, which depict a triangle-like symmetry indicating a combined battery behavior of the BP/C composite and capacitive behavior of the AC (Figure S11). The specific capacitance values of the BP/C-55//AC were 66, 58, 53, 51, and  $24 \text{ F g}^{-1}$  at current densities of 0.1, 0.2, 0.5, 1.0, and  $5.0 \text{ mA cm}^{-2}$ , respectively. In order to get deeper insights into the electrochemical performance of the BP/C-55//AC, the performance of each electrode was monitored. At the low current density  $0.5 \text{ mA cm}^{-2}$  (Figure 4a), with in discharge time 0.75 h (45 min), the positive electrode potential swings from 2.7 to 4.3 V (1.6 V) and the negative electrode potential swings from 2.2 to 0.07 V (2.13 V) when the current density is increased  $5.0 \text{ mA cm}^{-2}$  (Figure 4b), with an associated discharge time of 0.1 h (6 min), the potential of both positive and negative electrode almost unchanged. This means that, BP/C-55//AC is stable drive and negative electrode does not have the risk of lithium plating under full-cell condition.

BP/C-55//AC displayed appreciable cycling stability (Figure 4c), and a specific capacitance retention of 85% after 5000 cycles at a high current density of  $5.0 \text{ mA cm}^{-2}$  with a superior CE of nearly 100%. These results prove the efficiency of the BP-based LICs constructed using rationally designed BP composites, which achieves a high reversible charge/discharge rate and cycling stability.

Figure 4(d) shows the Ragone plots. The maximum energy density of BP/C-55//AC ( $178 \text{ Wh kg}^{-1}$ ) is similar to that of BP/C-73//AC ( $182 \text{ Wh kg}^{-1}$ ). The energy densities of both the BP-based LICs are similar at low current density because both BP/C-73 and BP/C-55 deliver higher capacities than the above-mentioned specific capacity (~ $1200 \text{ mAh g}^{-1}$ ). The maximum power density of BP/C-55//AC was  $3.0 \text{ kW kg}^{-1}$  at  $65 \text{ Wh kg}^{-1}$ , which is higher than that of BP/C-73//AC (maximum power density of  $2.7 \text{ W kg}^{-1}$  at  $50 \text{ Wh kg}^{-1}$ ). BP/C-55//AC exhibits excellent rate capability and cycling stability compared to BP/C-73//AC (Figure S10). The BP-based LICs with high energy and power density were comparable to previously reported carbonaceous material-based LICs.<sup>[63–69]</sup>

## Conclusion

A novel BP-based LIC is implemented by introducing a BP/C composite with chemical bonding incorporated in the embedded structure to improve rate capability and cycling stability. The composite exhibited a high capacity of  $1088 \text{ mAh g}^{-1}$  at  $5.0 \text{ A g}^{-1}$  and superior cycling stability up to 1000 cycles. The superior electrochemical performances are the results of improved electrical conductivity and mitigated volume expansion by embedded structure with BP in amorphous carbon and covalent bonding at interface. The optimized composite was used in anode materials for LICs, exhibiting a maximum energy density of  $178 \text{ Wh kg}^{-1}$  at  $32 \text{ W kg}^{-1}$ , maximum power density of  $3.0 \text{ kW kg}^{-1}$  at  $65 \text{ Wh kg}^{-1}$ , and specific capacitance retention of 85% after 5000 cycles at a high current density of  $5.0 \text{ mA cm}^{-2}$ . The BP has been successfully

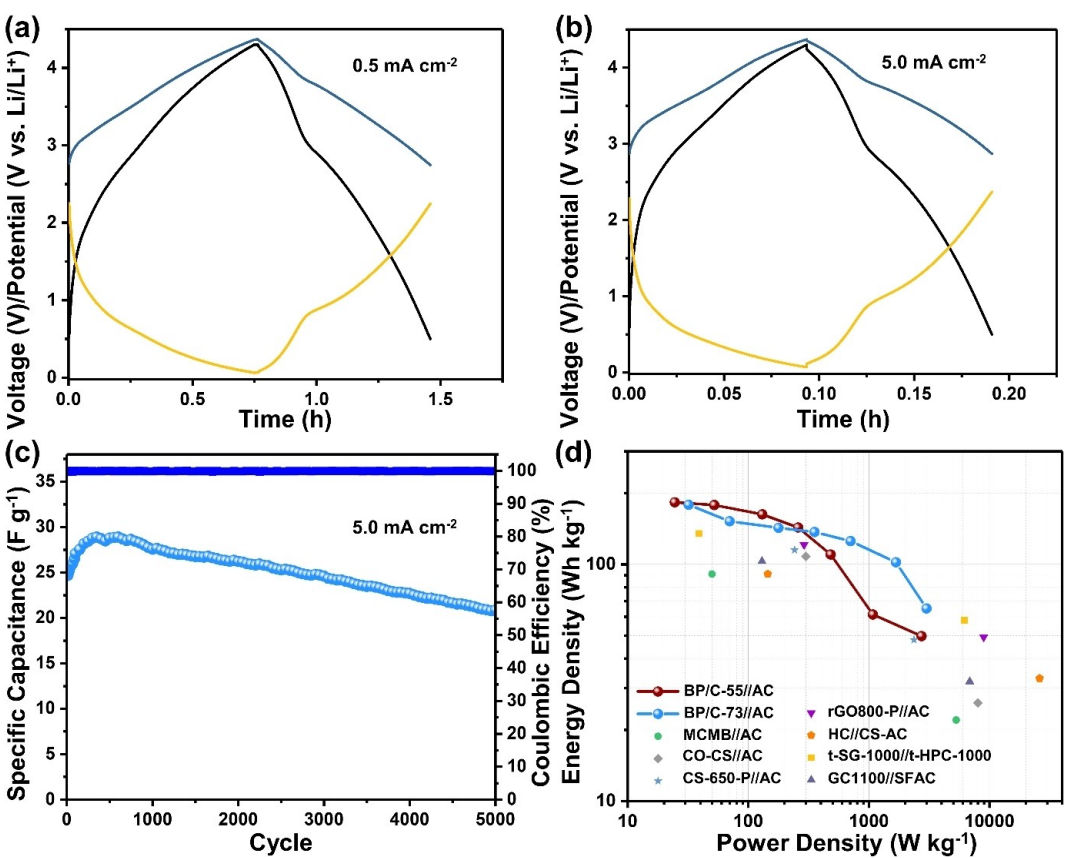


**Figure 4.** Electrochemical performance of BP-based LIC. The GCD profiles of BP/C-55//AC from 0.5 to 4.3 V at a) 0.5  $\text{mA cm}^{-2}$  (low current density) and b) 5.0  $\text{mA cm}^{-2}$  (high current density): LIC (black), positive electrode (blue), and negative electrode (yellow). c) Cycling stability of BP/C-55//AC at a current density of 5.0  $\text{mA cm}^{-2}$ . d) Ragone plots of BP-based LICs (BP/C-73//AC and BP/C-55//AC) compared with previously reported carbonaceous material-based LICs.

introduced into the anode of LIC and shows excellent performance. These remarkable results demonstrate the potential for the application of BP as an innovative anode material in LICs of EVs and other electrical components.

## Experimental Section

### Preparation of BP/C composites

Red phosphorus (RP, 250 mesh, 99.9% purity), used in this study as a starting material, was purchased from Alfa Aesar. RP (1.2 g) was ball-milled in a stainless-steel jar using a Fritsch Planetary Micro Mill Pulverisette 7 for 48 h under an argon atmosphere to obtain BP. The ball to powder ratio was 150:1 (ten balls of diameters 15 mm and 10 mm were used) and the rotation speed was set at 450 rpm. The obtained BP was mixed with CNTs in 7:3 and 5:5 weight ratios. Thereafter, 1 g of each mixture was milled using the same ball mill under identical conditions (300 rpm, 60:1, 48 h, 10/5 mm). The ball milled products (denoted as BP/C-73 and BP/C-55) were removed from the ball-milling container and handled in a glove box under an argon atmosphere.

### Materials characterization

The morphologies of the samples were examined using field-emission scanning electron microscopy (FE-SEM; JEOL, JSM-6700F, Japan), transmission electron microscopy (TEM; JEOL, JEM-2000EX, Japan), high angle annular dark field imaging (HAADF), and energy-dispersive X-ray spectroscopy (EDS) mapping. X-ray diffraction (XRD) data were collected from powder samples on a Rigaku D/Max 2500/PC instrument using a Cu  $K_{\alpha}$  radiation source ( $\lambda = 1.54181 \text{ \AA}$ ) operated at 40 kV and 30 mA. Thermogravimetric analysis (TGA, NETZSCH, Germany) was performed using an analyzer (NETZSCH, Germany) in an argon atmosphere at a heating rate of  $10^{\circ}\text{C min}^{-1}$  from 30 to  $900^{\circ}\text{C}$ . The crystalline graphitic layer intensity and disordered carbon peaks were confirmed by Raman spectrometry (HORIBA Jobin Yvon, LabRAM ARAMIS, Japan) using an Ar-ion laser beam. X-ray photoelectron spectroscopy (XPS) (PHI 5000 VersaProbe) was performed using monochromatic Al  $K_{\alpha}$  radiation.

### Electrochemical characterization

The electrodes for the anode were prepared using the BP and BP/C composites as the active materials, Super-P black (TIMCAL Graphite & Carbon Co., Belgium) as the conducting material, and poly(acrylic acid) (PAA, 2 wt % dispersion in distilled water, Aldrich) as the binder, with a corresponding weight ratio of 7:2:1. The slurries were spread onto Cu foils, and the coated electrodes were dried at

120 °C for 24 h in a vacuum oven. The electrodes were punched out in 12 mm-diameter pieces and the mass loading was controlled in the range of 0.5–0.6 mg cm<sup>-2</sup>. The electrodes for the cathode were prepared using activated carbon (AC, CEP21-KS, PCT, Korea) as the active material, Super-P black (TIMCAL Graphite & Carbon Co., Belgium) as the conducting material, and polytetrafluoroethylene (PTFE, 60 wt% dispersion in distilled water, Aldrich) as the binder, with a corresponding weight ratio of 90:5:5. The mixed and kneaded electrode materials were repeatedly rolled in a roll-press machine (heated at 60 °C) followed by drying at 200 °C for 24 h in a vacuum oven and finally punched using a 12 mm-diameter punch. Electrochemical tests were performed using a coin-cell (CR 2032) configuration in a dry room at 25 °C. A microporous polyethylene film (Celgard 2400) was used as the separator, and the electrolyte was 1 M LiPF<sub>6</sub> dissolved in a mixture of ethylene carbonate (EC) and dimethyl carbonate (DMC) in a 1:1 volume ratio; 10 vol% fluoroethylene carbonate (FEC) acted as the additive. LICs were also assembled in coin cells with pre-lithiated BP/C composites as the anodes, activated carbon (AC) as the cathodes, and Celgard 2400 membranes as the separators. Additionally, to confirm behavior of negative and positive electrode, LICs were assembled using pre-lithiated BP/C-55 as negative electrode vs. activated carbon as positive electrode in a three electrode Swagelok-type cell, using metallic lithium as reference electrode. To adjust the mass ratio between the anode and cathode, the average mass loading of the anodes was controlled at approximately 0.43–0.44 mg and the corresponding loading of the cathodes ranged from to 7.50–7.51 mg. The specific capacitances were calculated based on the weights of the active materials in the negative and positive electrodes. All the above-mentioned tests were performed at 25 °C. Galvanostatic charge/discharge (GCD) profiles were obtained using a battery test system (WonAtech, Korea). Cyclic voltammetry (CV) was performed using an electrochemical workstation (Bio-Logic SAS VSP), negative electrode 0.05–2.0 V (vs. Li/Li<sup>+</sup>), positive electrode 2.5–4.3 V (vs. Li/Li<sup>+</sup>) were applied for the half-cell anode and voltages of 0.5–4.3 V were used for the full cells. Before fabricating a full-cell, the anode was pre-lithiated via the electrochemical method. The assembled half-cell had a cut off potential of 0.6 V at 0.1 mA g<sup>-1</sup>, and then maintained a constant potential of 0.6 V for 20 h. The current of the full cells was calculated based on the mass of the anode material. The specific energy density (*E*, Wh kg<sup>-1</sup> and power density (*P*, W kg<sup>-1</sup>) were calculated using Equations (1) and (2):

$$E = \int_{t_2}^{t_1} IVdt \quad (1)$$

$$P = E\Delta t \quad (2)$$

where *I* represent the discharge current (A), *m* denotes the mass of the anode and cathode (kg), *t* stands for the discharge time (h), and *V* signifies the discharge voltage (V).

## Acknowledgements

This work was supported by the Technology Innovation Program (20010829, Development of a supercapacitor (16D×25 L) in 3.0 V 85 °C for Smart Meter (AMI)) funded by the Ministry of Trade, Industry & Energy (MOTIE, Korea) and by the National R&D Program through the National Research Foundation of Korea (NRF) funded by Ministry of Science and ICT (2021M3H4A3A02086100).

## Conflict of Interest

The authors declare no conflict of interest.

## Data Availability Statement

The data that support the findings of this study are available in the supplementary material of this article.

**Keywords:** amorphous carbon · black phosphorus · chemical bonding · embedded structure · lithium-ion capacitor

- [1] S. Manoharan, K. Krishnamoorthy, A. Sathyaseelan, S.-J. Kim *Mater. Chem. Front.* **2021**, 6200–6211.
- [2] X. Wang, S. Li, W. Zhang, D. Wang, Z. Shen, J. Zheng, H. L. Zhuang, Y. He, Y. Lu *Nano Energy* **2021**, 89, 106353.
- [3] Y. Liu, P. R. Shearing, G. He, D. J. Brett, Ed. 1 (Eds: Y. Gao, W. Song, J. L. Liu, S. Bashir), Springer Nature, Cham, Switzerland 2021, Ch. 15.
- [4] J. J. Lamb, O. S. Burheim *Energies* **2021**, 14, 979.
- [5] S. Dong, N. Lv, Y. Wu, G. Zhu, X. Dong *Adv. Funct. Mater.* **2021**, 31, 2100455.
- [6] L. F. Zhao, Z. Hu, W. H. Lai, Y. Tao, J. Peng, Z. C. Miao, Y. X. Wang, S. L. Chou, H. K. Liu, S. X. Dou *Adv. Energy Mater.* **2021**, 11, 2002704.
- [7] D. Yan, S.-H. Li, L.-P. Guo, X.-L. Dong, Z.-Y. Chen, W.-C. Li *ACS Appl. Mater. Interfaces* **2018**, 10, 43946–43952.
- [8] Y. An, T. Liu, C. Li, X. Zhang, T. Hu, X. Sun, K. Wang, C. Wang, Y. Ma *J. Mater. Chem. A* **2021**, 9, 15654–15664.
- [9] X. Sun, L. Geng, S. Yi, C. Li, Y. An, X. Zhang, X. Zhang, K. Wang, Y. Ma *J. Power Sources* **2021**, 499, 229936.
- [10] D. Yarmolich, Y. Odarchenko, C. Murphy, E. A. Petrucco, J. Cookson, D. Yarmolich, T. Zhao, H.-K. Kim, R. V. Kumar, R. I. Tomov *Nano Energy* **2021**, 83, 105816.
- [11] M. X. Tran, A.-Y. Kim, J. K. Lee *Appl. Surf. Sci.* **2018**, 461, 161–170.
- [12] M. Ben-Marzouk, S. Pelissier, G. Clerc, A. Sari, P. Venet *IEEE Trans. Veh. Technol.* **2021**, 70, 5618–5627.
- [13] X.-I. Shen, Z.-j. Li, N.-p. Deng, J. Fan, L. Wang, Z.-p. Xia, W.-m. Kang, Y. Liu *Chem. Eng. J.* **2020**, 387, 124058.
- [14] J. Hwang, W. Zhang, S. Youk, K. Schutjajew, M. Oschatz *Energy Technol.* **2021**, 9, 2001054.
- [15] L.-Q. Sun, M.-J. Li, K. Sun, S.-H. Yu, R.-S. Wang, H.-M. Xie *J. Phys. Chem. C* **2012**, 116, 14772–14779.
- [16] H. Jin, S. Xin, C. Chuang, W. Li, H. Wang, J. Zhu, H. Xie, T. Zhang, Y. Wan, Z. Qi *Science* **2020**, 370, 192–197.
- [17] H. Liu, L. Tao, Y. Zhang, C. Xie, P. Zhou, H. Liu, R. Chen, S. Wang *ACS Appl. Mater. Interfaces* **2017**, 9, 36849–36856.
- [18] F. Wu, J. Maier, Y. Yu *Chem. Soc. Rev.* **2020**, 49, 1569–1614.
- [19] M. Rajapakse, R. Musa, U. O. Abu, B. Karki, M. Yu, G. Sumanasekera, J. B. Jasinski *J. Phys. Chem. C* **2020**, 124, 10710–10718.
- [20] W. Xia, Q. Zhang, F. Xu, H. Ma, J. Chen, K. Qasim, B. Ge, C. Zhu, L. Sun *J. Phys. Chem. C* **2016**, 120, 5861–5868.
- [21] Z. Yue, T. Gupta, F. Wang, C. Li, R. Kumar, Z. Yang, N. Koratkar *Carbon* **2018**, 127, 588–595.
- [22] J. Song, Z. Yu, M. L. Gordin, X. Li, H. Peng, D. Wang *ACS Nano* **2015**, 9, 11933–11941.
- [23] X. Ma, L. Chen, X. Ren, G. Hou, L. Chen, L. Zhang, B. Liu, Q. Ai, L. Zhang, P. Si *J. Mater. Chem. A* **2018**, 6, 1574–1581.
- [24] J. Sun, G. Zheng, H.-W. Lee, N. Liu, H. Wang, H. Yao, W. Yang, Y. Cui *Nano Lett.* **2014**, 14, 4573–4580.
- [25] D. S. Su, R. Schlögl *ChemSusChem* **2010**, 3, 136–168.
- [26] L. Xiao, Y. Cao, J. Xiao, W. Wang, L. Kovarik, Z. Nie, J. Liu *Chem. Commun.* **2012**, 48, 3321–3323.
- [27] J. Leibowitz, E. Allcorn, A. Manthiram *J. Power Sources* **2015**, 279, 549–554.
- [28] J. D. Wood, S. A. Wells, D. Jariwala, K.-S. Chen, E. Cho, V. K. Sangwan, X. Liu, L. J. Lauhon, T. J. Marks, M. C. Hersam *Nano Lett.* **2014**, 14, 6964–6970.
- [29] T. Zhang, Y. Wan, H. Xie, Y. Mu, P. Du, D. Wang, X. Wu, H. Ji, L. Wan *J. Am. Chem. Soc.* **2018**, 140, 7561–7567.

- [30] Y. Abate, D. Akinwande, S. Gamage, H. Wang, M. Snure, N. Poudel, S. B. Cronin *Adv. Mater.* **2018**, *30*, 1704749.
- [31] Y. Zhou, F. Chu, S. Qiu, W. Guo, S. Zhang, Z. Xu, W. Hu, Y. Hu *J. Hazard. Mater.* **2020**, *399*, 123015.
- [32] J. Song, Z. Yu, M. L. Gordin, S. Hu, R. Yi, D. Tang, T. Walter, M. Regula, D. Choi, X. Li *Nano Lett.* **2014**, *14*, 6329–6335.
- [33] S. Wild, X. T. Dinh, H. Maid, F. Hauke, G. Abellán, A. Hirsch *Angew. Chem. Int. Ed.* **2020**, *59*, 20230–20234; *Angew. Chem.* **2020**, *132*, 20406–20411; *Angew. Chem.* **2020**, *132*, 20406–20411.
- [34] C. R. Ryder, J. D. Wood, S. A. Wells, Y. Yang, D. Jariwala, T. J. Marks, G. C. Schatz, M. C. Hersam *Nat. Chem.* **2016**, *8*, 597–602.
- [35] P. Ladpli, R. Nardari, F. Kopsaftopoulos, F.-K. Chang *J. Power Sources* **2019**, *414*, 517–529.
- [36] J. Cui, F. Cheng, J. Lin, J. Yang, K. Jiang, Z. Wen, J. Sun *Powder Technol.* **2017**, *311*, 1–8.
- [37] Y. Zhang, Y. Wei, H. Li, Y. Zhao, F. Yin, X. Wang *Mater. Lett.* **2016**, *184*, 235–238.
- [38] D. Zhang, K. Zhang, Y. Yao, F. Liang, T. Qu, W. Ma, B. Yang, Y. Dai, Y. Lei *Fullerenes Nanotubes Carbon Nanostruct.* **2019**, *27*, 746–754.
- [39] Z. Shen, S. Sun, W. Wang, J. Liu, Z. Liu, C. Y. Jimmy *J. Mater. Chem. A* **2015**, *3*, 3285–3288.
- [40] A. Cao, C. Xu, J. Liang, D. Wu, B. Wei *Chem. Phys. Lett.* **2001**, *344*, 13–17.
- [41] Y. Chen, J. F. Gerald, J. Williams, S. Bulcock *Chem. Phys. Lett.* **1999**, *299*, 260–264.
- [42] S. Liu, N. Huo, S. Gan, Y. Li, Z. Wei, B. Huang, J. Liu, J. Li, H. Chen *J. Mater. Chem. C* **2015**, *3*, 10974–10980.
- [43] H. B. Ribeiro, M. A. Pimenta, C. J. De Matos, R. L. Moreira, A. S. Rodin, J. D. Zapata, E. A. De Souza, A. H. Castro Neto *ACS Nano* **2015**, *9*, 4270–4276.
- [44] H. Li, K. Yue, Z. Lian, Y. Zhan, L. Zhou, S. Zhang, Z. Shi, Z. Gu, B. Liu, R. Yang *Appl. Phys. Lett.* **2000**, *76*, 2053–2055.
- [45] A. Cuesta, P. Dhamelincourt, J. Laureyns, A. Martinez-Alonso, J. D. Tascón *Carbon* **1994**, *32*, 1523–1532.
- [46] A. C. Ferrari, J. Robertson *Phys. Rev. B* **2000**, *61*, 14095.
- [47] J. Schwan, S. Ulrich, V. Batori, H. Ehrhardt, S. Silva *J. Appl. Phys.* **1996**, *80*, 440–447.
- [48] S. Liang, G. Li, R. Tian *J. Mater. Sci.* **2016**, *51*, 3513–3524.
- [49] S. Bhattacharyya, C. Cardinaud, G. Turban *J. Appl. Phys.* **1998**, *83*, 4491–4500.
- [50] X. Xia, L. Liu, X. Li, S. Gao, T. Yang *J. Catal.* **2019**, *374*, 401–408.
- [51] Y. Liu, P. Gao, T. Zhang, X. Zhu, M. Zhang, M. Chen, P. Du, G. W. Wang, H. Ji, J. Yang *Angew. Chem.* **2019**, *131*, 1493–1497; *Angew. Chem. Int. Ed.* **2019**, *58*, 1479–1483; *Angew. Chem. Int. Ed.* **2019**, *58*, 1479–1483.
- [52] T. Zhou, H. Ni, Y. Wang, C. Wu, H. Zhang, J. Zhang, A. P. Tomśia, L. Jiang, Q. Cheng *Proc. Nat. Acad. Sci.* **2020**, *117*, 8727–8735.
- [53] Y. Shi, Z. Yi, Y. Kuang, H. Guo, Y. Li, C. Liu, Z. Lu *Chem. Commun.* **2020**, *56*, 11613–11616.
- [54] Z. Yang, J. Hao, S. Yuan, S. Lin, H. M. Yau, J. Dai, S. P. Lau *Adv. Mater.* **2015**, *27*, 3748–3754.
- [55] S. Fan, J. Qiao, J. Lai, H. Hei, Z. Feng, Q. Zhang, D. Zhang, S. Wu, X. Hu, D. Sun *ACS Appl. Mater. Interfaces* **2019**, *11*, 9213–9222.
- [56] X. Li, G. Chen, Z. Le, X. Li, P. Nie, X. Liu, P. Xu, H. B. Wu, Z. Liu, Y. Lu *Nano Energy* **2019**, *59*, 464–471.
- [57] S. Haghhighat-Shishavan, M. Nazarian-Samani, M. Nazarian-Samani, H.-K. Roh, K.-Y. Chung, B.-W. Cho, S. F. Kashani-Bozorg, K.-B. Kim *J. Mater. Chem. A* **2018**, *6*, 10121–10134.
- [58] H. Liu, Y. Zou, L. Tao, Z. Ma, D. Liu, P. Zhou, H. Liu, S. Wang *Small* **2017**, *13*, 1700758.
- [59] Y. Zhang, L. Wang, H. Xu, J. Cao, D. Chen, W. Han *Adv. Funct. Mater.* **2020**, *30*, 1909372.
- [60] Q. Jiang, J. Li, N. Yuan, Z. Wu, J. Tang *Electrochim. Acta* **2018**, *263*, 272–276.
- [61] X. Wu, W. Zhao, H. Wang, X. Qi, Z. Xing, Q. Zhuang, Z. Ju *J. Power Sources* **2018**, *378*, 460–467.
- [62] U. Kasavajjula, C. Wang, A. J. Appleby *J. Power Sources* **2007**, *163*, 1003–1039.
- [63] Z. Yang, H. Guo, X. Li, Z. Wang, Z. Yan, Y. Wang *J. Power Sources* **2016**, *329*, 339–346.
- [64] S. Jayaraman, S. Madhavi, V. Aravindan *J. Mater. Chem. A* **2018**, *6*, 3242–3248.
- [65] S. Jiang, Q. Ji, S. Yun, Z. Zhang, Q. Jiang, H. C. Chen *J. Energy Storage* **2021**, *39*, 102625.
- [66] G. Moreno-Fernández, M. Granados-Moreno, J. L. Gómez-Urbano, D. Carriazo *Batteries & Supercaps* **2021**, *4*, 386–386.
- [67] S. Jayaraman, A. Jain, M. Ulaganathan, E. Edison, M. Srinivasan, R. Balasubramanian, V. Aravindan, S. Madhavi *Chem. Eng. J.* **2017**, *316*, 506–513.
- [68] J. Wang, Z. Yan, G. Yan, H. Guo, X. Li, Z. Wang, X. Wang, Z. Yang *Energy Storage Mater.* **2021**, *38*, 528–534.
- [69] Z. Yang, H. Guo, X. Li, Z. Wang, J. Wang, Y. Wang, Z. Yan, D. Zhang *J. Mater. Chem. A* **2017**, *5*, 15302–15309.
- [70] N.-W. Li, X. Du, J.-L. Shi, X. Zhang, W. Fan, J. Wang, S. Zhao, Y. Liu, W. Xu, M. Li *Electrochim. Acta* **2018**, *281*, 459–465.

Manuscript received: January 17, 2022

Version of record online: March 1, 2022